Spin-orbit-driven transitions between Mott insulators and finite-momentum superfluids of bosons in optical lattices

Mi Yan,[1] Yinyin Qian,[2] Hoi-Yin Hui,[1] Ming Gong,[2,3,4] Chuanwei Zhang,[2,*] and V. W. Scarola[1]

[1]*Department of Physics, Virginia Tech, Blacksburg, Virginia 24061, USA*

[2]*Department of Physics, The University of Texas at Dallas, Richardson, Texas 75080, USA*

[3]*Key Lab of Quantum Information, CAS, University of Science and Technology of China, Hefei 230026, People's Republic of China*

[4]*Synergetic Innovation Center of Quantum Information and Quantum Physics, University of Science and Technology of China, Hefei 230026, People's Republic of China*

(Received 18 December 2016; revised manuscript received 3 October 2017; published 13 November 2017)

Synthetic spin-orbit coupling in ultracold atomic gases can be taken to extremes rarely found in solids. We study a two-dimensional Hubbard model of bosons in an optical lattice in the presence of spin-orbit coupling strong enough to drive direct transitions from Mott insulators to superfluids. Here we find phase-modulated superfluids with finite momentum that are generated entirely by spin-orbit coupling. We investigate the rich phase patterns of the superfluids, which may be directly probed using time-of-flight imaging of the spin-dependent momentum distribution.

DOI: 10.1103/PhysRevA.96.053619

I. INTRODUCTION

The Rashba effect [1] in solids derives from the motion of an electron in a strong electric field. As the electron moves in the presence of a potential gradient, ∇V, it experiences an effective magnetic field in its frame of reference. The Rashba energy [1]

$$(\vec{\nabla} V \times \vec{p}) \cdot \vec{\sigma}, \tag{1}$$

captures the energetics of electron spin reorientation due to the effective magnetic field, where $\vec{p}$ is the particle momentum and $\vec{\sigma}$ are the Pauli matrices. The Rashba spin-orbit coupling (SOC) energy is well known to be particularly strong at metallic surfaces [2,3] [e.g., on Ag(111) or Au(111)] because here we find extremely strong potential gradients. As a result, studies of the impact of Rashba SOC on two-dimensional (2D) conductors have a long history [4]. But the impact of Rashba SOC on the surface states of Mott insulators has come under more careful scrutiny recently because of possible connections to topological insulators [5,6].

Mott insulators localize as a result of strong interaction and would therefore appear to exclude the possibility of SOC effects, but one can argue that this is not always the case. Small momentum in Eq. (1) (the case for localized states) does not necessarily imply low Rashba energies. In an extreme limit, Mott insulating surfaces can, in principle, experience very large potential gradients that can compensate the small momentum, i.e., $\langle p \rangle \to 0$ with $\langle \vec{\nabla} V \times \vec{p} \rangle \sim E_F$, where E_F is the Fermi energy. If, in this limit, the energetics of Rashba SOC compete with the Mott gap, one could observe a transition between a Mott insulator and a conducting state driven entirely by Rashba SOC in spite of the small average momentum of particles in Mott insulators. Unfortunately, the limit where Rashba SOC competes with the Mott gap is rare in solids because it would typically be precluded by other effects, such as charge transfer between bands. But this limit can be explored in another context: using synthetic SOC in optical lattices.

Recent experimental progress [7–13] demonstrates engineering of synthetic SOC for ultracold atomic gases [14]. These experiments show that Raman beams can be used to dress atoms with a spin-dependent momentum. Rashba (and/or Dresselhaus) SOCs governing these dressed states [15,16] are tunable to extremes not possible in solids (see Fig. 1). Recent work shows, for example, that synthetic SOC can generate flatbands [17–20], exotic superfluidity [21], and intriguing vortex structures [16,22,23].

Recent theory work has also explored the impact of SOC on the spin structure of Mott insulators in optical lattices [24–28]. Here superexchange coupling between sites was shown to combine with Rashba SOC to lead to rich spin structures within the Mott state [24–28]. But in these studies parameters were chosen to explore the impact of Rashba SOC on the spin physics of Mott insulators while leaving the charge structure intact.

In this work we explore Rashba SOC that is strong enough to cause the breakdown of charge ordering in Mott insulators. This extreme limit is of direct relevance to optical lattice experiments with synthetic SOC. We study, in particular, a 2D lattice model of two-component interacting bosons in the presence of tunable Rashba coupling. We find that strong Rashba SOC can cause the breakdown of the Mott insulating state and drive a direct transition between the Mott insulator and a superfluid state, even in the *absence* of single-particle tunneling between sites of the lattice [27]. This limit is the lattice version of the limit discussed above, $\langle p \rangle \to 0$ with $\langle \vec{\nabla} V \times \vec{p} \rangle \sim E_F$, where vanishing kinetics leaves Rashba SOC to generate its own conducting state. For the case of lattice bosons studied here, we find that Rashba SOC generates finite momentum superfluids. We show that these superfluids are characterized by staggered phase patterns. We also find distinct superfluid states with striped phase patterns that are separated by transitions on finite lattices with periodic boundaries. We predict that finite momentum superfluids should be observable in time-of-flight measurements of the momentum distribution.

The paper is organized as follows: In Sec. II we construct a Bose-Hubbard model of two-component atoms in the presence of Rashba SOC. We also discuss two complimentary

*chuanwei.zhang@utdallas.edu

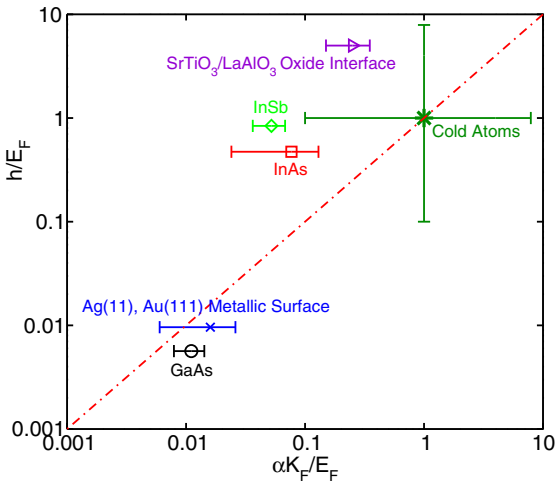

FIG. 1. Comparison of SOC strengths in solids and cold atoms. h, α, and E_F denote the Zeeman energy, SOC coefficient, and Fermi energy, respectively. For GaAs, the effective mass is $m^* = 0.067m_0$ [29], where m_0 is the electron mass, the Rashba SOC strength is $\alpha = (0.04\text{–}0.06) \times 10^{-11}$ eV m [30], and the g factor is $g^* = -0.45$ [31]. For InAs the parameters are $m^* = 0.026m_0$ [29], $\alpha = (0.28\text{–}1.4) \times 10^{-11}$ eV m [32], and $g^* = -15.1$ [33]. For InSb the parameters are $m^* = 0.0135$ [29], $\alpha K_F = (1.0\text{–}1.2) \times 10^{-11}$ eV m [34], and $g^* = -51$ [33]. And for the metallic surfaces $m^* \sim 0.255m_0$ [2,3], where the g factor is assumed to be $g^* = 2$. The parameters for these four different examples are plotted at an external magnetic field of 5 Tesla. A high carrier density, $n = 10^{11}$ cm^{-2}, is used for the semiconductors. For $SrTiO_3/LaAlO_3$ oxide interfaces, the data are taken from Ref. [35]. Additional feasible parameter regimes are plotted as horizontal and vertical bars.

mean-field approaches that allow us to compute the phase diagram, transition properties, and the momentum distribution. In Sec. III we present results on finite lattice sizes. We use Gutzwiller mean-field theory to show that Rashba SOC causes the bosonic Mott insulator to give way to finite momentum superfluids. We also explore inter-superfluid transitions. We find that transitions separate distinct phase patterns of finite momentum superfluids. We demonstrate in Sec. IV that these different finite momentum phases can indeed be observed in experiments with a trapping potential. In Sec. V we present analytic arguments that transitions depend critically on boundary effects, akin to effects found in Fulde-Ferrell-Larkin-Ovchinnikov (FFLO) superconductors [36–47]. We show that analytic mean-field calculations in the infinite system size limit do not show these transitions. We summarize in Sec. VI.

II. MODEL AND METHODS

We consider a 2D square optical lattice containing bosonic atoms with two hyperfine levels. States with two hyperfine levels act as a pseudospin-1/2 state. We also assume the presence of Raman beams that couple the atomic momentum to the spin to generate synthetic SOC [7–11,13]. The interaction between alkali-metal atoms is governed by a short-range (s-wave) repulsion. For a deep optical lattice, the problem can be accurately described in the single-band, tight-binding

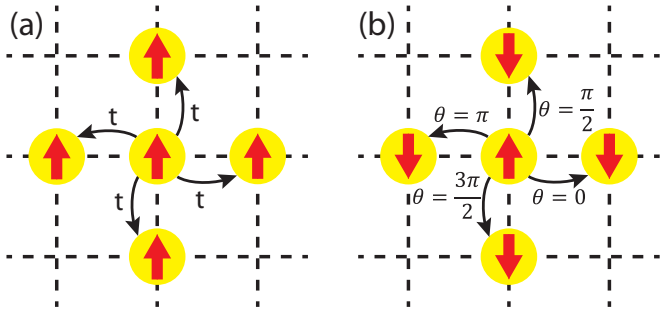

FIG. 2. Schematic of spin-independent tunneling (a) and spin-dependent tunneling induced by SOC (b). In the latter case, the tunneling takes place between two neighboring sites accompanied by both spin flipping and phase variations. The phase variation during tunneling is responsible for the creation of the finite momentum superfluids.

limit [48] where the s-wave interaction becomes an on-site Hubbard interaction and the SOC is discretized.

To study this system we construct a Hubbard model of two-component bosons in the presence of Rashba SOC on a square lattice. We allow the on-site Hubbard interaction to have a spin-dependent interaction:

$$H = -t \sum_{\langle ij \rangle} \Psi_i^\dagger \Psi_j + \frac{U}{2} \sum_{i\sigma} n_{i\sigma}(n_{i\sigma} - 1) + U_{\uparrow\downarrow} \sum_i n_{i\uparrow} n_{i\downarrow} - \mu \sum_{i\sigma} n_{i\sigma} + i\lambda \sum_{\langle ij \rangle} \Psi_i^\dagger \vec{e}_z \cdot (\vec{\sigma} \times \vec{d}_{ij}) \Psi_j + \text{H.c.}, \quad (2)$$

where $\Psi_i = (b_{i\uparrow}, b_{i\downarrow})^T$ is a two-component bosonic annihilation operator at the site i, $n_{i\sigma} = b_{i\sigma}^\dagger b_{i\sigma}$, t is the spin-independent nearest-neighbor tunneling, U ($U_{\uparrow\downarrow}$) is the on-site interaction between bosons of the same (different) spin σ, and μ is the chemical potential. In the last term λ is the Rashba SOC strength, $\vec{d}_{ij}$ is the unit vector between the neighboring sites i and j, and $\vec{e}_z$ is the unit vector along the z direction. In the following we use $U = 1$ to set the energy scale.

The tunneling and Rashba terms induce two *different* types of superfluidity. To see this we plot the spin-independent tunneling and spin-dependent tunneling in Fig. 2. The left panel shows that the spin-independent tunneling favors phase uniformity since t is real. But in the right panel we see that SOC has two effects: It induces tunneling between neighboring sites with two different spin states and it imposes phase variation. The phase variation depends strongly on the direction of the neighboring sites. SOC therefore favors highly anisotropic superfluid states. Without SOC the system has at least a U(1) $\otimes$ U(1) symmetry, which means that the total number of each species is conserved; however, SOC introduces spin flips between two neighboring sites, thus the system only respects U(1) symmetry and, as a result, the phase difference between the neighboring sites cannot be gauged out. The competition between spin-independent tunneling and spin-dependent tunneling tunes the transition between these different superfluids.

In the weakly interacting limit the model exhibits three different superfluid phases: In the regime when spin-independent tunneling dominates ($t \gg \lambda$), the uniform superfluid is preferred and the total momentum of the superfluid is zero. In the opposite regime, a staggered superfluid phase is preferred; and in the intermediate regime, $t \sim \lambda$, the strong competition between the two tunnelings gives rise to superfluids with phase patterns that depend strongly on boundary effects.

Strong interactions add competing Mott insulating phases and complicates estimates of the phase diagram. To study the competition between all ground states we use two complimentary mean-field approaches. We apply the Gutzwiller mean-field method to finite system sizes (relevant to experiments) and compare with an otherwise equivalent mean-field method applied to infinite system sizes.

We now discuss the Gutzwiller mean-field method [48,49]. The method assumes a product ground state of the form $|G\rangle = \prod_{i,\sigma}(\sum_n f_n^{(i,\sigma)}|n\rangle_{i,\sigma})$. This form for the wave function has been extensively applied to bosons in optical lattices [48], even in the presence of complex hopping amplitudes [50]. It generally gives quantitatively reliable results in 2D and 3D (for comparisons, see, e.g., Ref. [51]), and is a particularly excellent approximation when computing local correlation functions (see, e.g., Ref. [52]). The variational parameters f are obtained by minimizing the total energy:

$$E = \frac{\langle G|H|G\rangle}{\langle G|G\rangle}. \tag{3}$$

We minimize the total ground-state energy with the conjugate gradient algorithm [53,54]. The ground-state energy is reached when the energy variation is less than $10^{-5}U$, which is sufficient to distinguish the energy difference between different phases.

We supplement the finite system size Gutzwiller method with an equivalent mean-field limit applied to infinite system sizes. We assume $\langle b_{i\sigma}\rangle = \psi e^{i\theta_{i\sigma}}$, where ψ is a real number. This assumption is equivalent to the assumed form for $|G\rangle$ but works best on infinite system sizes. The total energy then becomes

$$E_\psi = (U + U_{\uparrow\downarrow})\psi^4 - (U + 2\mu + tA + \lambda B)\psi^2, \tag{4}$$

where the coefficients are

$$A \equiv N^{-1}\sum_{\langle ij\rangle}[e^{i(\theta_{j\uparrow}-\theta_{i\uparrow})} + e^{i(\theta_{j\downarrow}-\theta_{i\downarrow})} + \text{H.c.}], \tag{5}$$

and

$$B \equiv N^{-1}\sum_{\langle ij\rangle}[Z_{ij}^* e^{i(\theta_{j\downarrow}-\theta_{i\uparrow})} - Z_{ij} e^{i(\theta_{j\uparrow}-\theta_{i\downarrow})} + \text{H.c.}], \tag{6}$$

with $Z_{ij} \equiv d_{ij}^x + i d_{ij}^y$ and N is the number of sites. An important point here is that the total energy depends not only on the magnitude of the order parameter ψ, but also on the phase difference between neighboring sites. We see that the minimal energy E_ψ corresponds to a maximal value of A and B when $U, U_{\uparrow\downarrow}, \lambda$, and t assume positive values (the case studied in this paper). Here A depends only on the phase difference between the same spin states, while B depends strongly on the phase difference between spin-up and spin-down states in the neighboring sites. The competition between A and B governs competition between superfluids with distinct phase patterns. When $\lambda = 0$, A takes its maximum value when all of the sites have the same phase, which corresponds to the uniform superfluid phase.

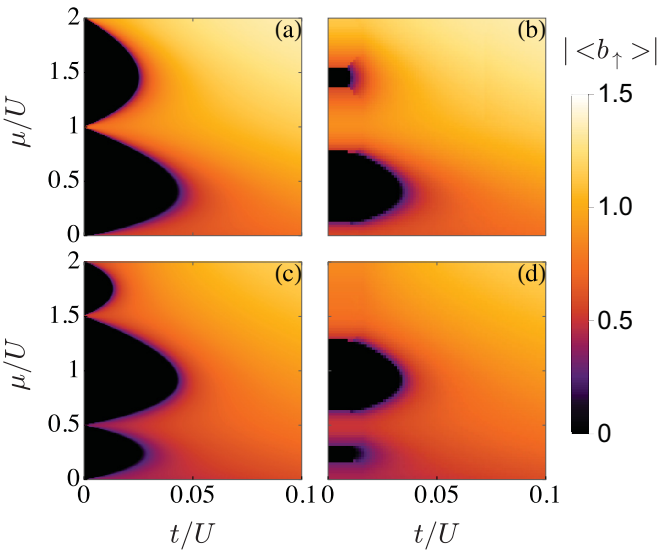

FIG. 3. Phase diagrams of of Eq. (2) obtained from Gutzwiller variational simulations for an 8×8 lattice with periodic boundary condition at (a) $U_{\uparrow\downarrow} = 0$, $\lambda = 0$, (b) $U_{\uparrow\downarrow} = 0$, $\lambda = 0.04U$, (c) $U_{\uparrow\downarrow} = 0.5U$, $\lambda = 0$, and (d) $U_{\uparrow\downarrow} = 0.5U$, $\lambda = 0.04U$. The phase diagrams are determined by the amplitude of the spin-up superfluid order parameter. The spin-down superfluid order parameter produces similar results.

III. QUANTUM PHASES IN FINITE LATTICES WITH PERIODIC BOUNDARIES

We now discuss results that demonstrate the competition between various Mott and superfluid phases in the presence of SOC. We first present our results on small system sizes with periodic boundaries. These system sizes are consistent with small states formed in the center of traps in experiments.

Figure 3 shows the phase diagram for four different limits of the model, Eq. (2). Figure 3(a) plots the Bose-Hubbard phase diagram [55] that results from setting the SOC term and the interspin interaction term to zero in Eq. (2), i.e., $\lambda = U_{\uparrow\downarrow} = 0$. The absence of interspin interactions allows two identical copies of the Mott insulator. The lower and upper Mott lobes in Fig. 3(a) correspond to $\langle n_{i\uparrow}\rangle = \langle n_{i\downarrow}\rangle = 1$ and $\langle n_{i\uparrow}\rangle = \langle n_{i\downarrow}\rangle = 2$, respectively.

Figure 3(c) shows the result of adding interspin repulsion, $U_{\uparrow\downarrow} > 0$, but with no SOC, $\lambda = 0$. Here we see that that the original low-energy Mott lobe is pushed up. The appearance of the small Mott lobes (above and below the larger Mott lobe) correspond to the formation of Mott insulators with Ising-type spin ordering. To see this, we rewrite the interaction terms in H using sum and difference operators, $n_{i\pm} \equiv n_{i\uparrow} \pm n_{i\downarrow}$. The large Mott lobe in Fig. 3(c) then corresponds to $\langle n_{i+}\rangle = 2$, $\langle n_{i-}\rangle = 0$. The upper and lower small Mott lobes exhibit degeneracies (for $t = 0$) and correspond to $\langle n_{i+}\rangle = 3, \langle n_{i-}\rangle = \pm 1$ and $\langle n_{i+}\rangle = 1, \langle n_{i-}\rangle = \pm 1$, respectively. Here we exclude superexchange effects, $O(t^2/U)$, discussed in other work [24–26,28].

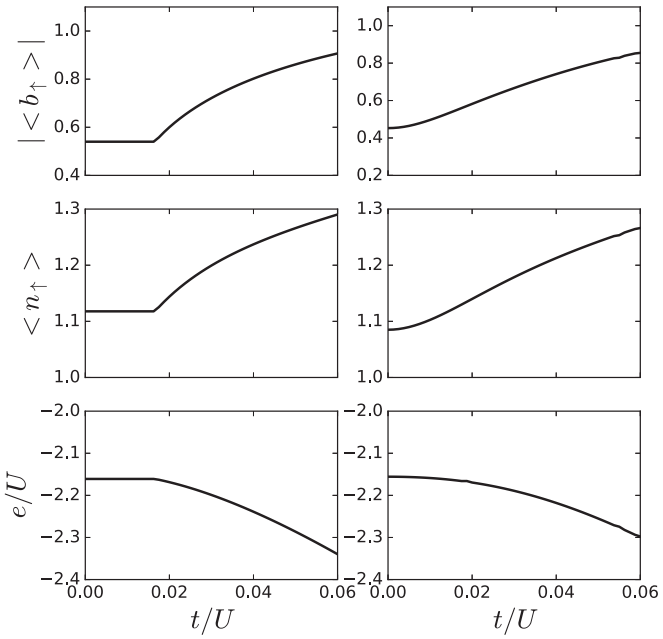

FIG. 4. Plot of the amplitude of spin-up superfluid order parameter $|\langle b_\uparrow \rangle|$, the filling factor $\langle n_\uparrow \rangle$, and the energy density e as a function of the spin-independent tunneling at $U_{\uparrow\downarrow} = 0.5U$, $\lambda = 0.04U$, and $\mu = 1.33U$ for periodic (left panel) and open (right panel) boundary conditions.

We now discuss the phase diagram that results from adding SOC. Figsures 3(b) and 3(d) plot the phase diagrams that result from adding SOC to the states depicted in Figs. 3(a) and 3(c), respectively. In both figures we see that the Mott insulators at higher μ vanish. Increasing μ causes a direct transition from a Mott insulator to a SOC-generated superfluid. At $t = 0$, SOC *alone* drives the formation of a superfluid. We find that the Mott insulators that normally persist at $t = 0$ for all μ are actually supplanted by SOC-generated superfluids. The $t = 0$ superfluids found on this part of the phase diagram derive kinetics purely from the spin-dependent tunneling in SOC. We therefore find that even in the limit of vanishing kinetics, the Rashba effect drives the Mott insulator into a conducting state (in this case, a superfluid state). We have also checked the phase diagrams of 4×4 and 6×6 lattices, and find no qualitative difference with an 8×8 lattice shown in Fig. 3. Below we show that the precise nature of the resulting superfluid depends on the relative strengths of λ and t, as well as boundary effects.

Figure 4 shows the transitions of different superfluid phase patterns. The left column shows the order parameters for the 8×8 lattice with periodic boundary conditions. Here SOC dominates and the nonzero order parameters are unchanged for $t \leqslant 0.019U$. For $t > 0.019U$, the order parameter gradually increases with t, which indicates a transition between different superfluids at $t \sim 0.019U$. For the open boundary condition case shown in the right column, there is no such transition since the phase can vary smoothly over the lattice.

The superfluids with different phase patterns have different momenta. To see this, we compute the spin-dependent momentum distribution at wave vector k:

$$\langle \rho_{\uparrow,\downarrow}(\vec{k}) \rangle = N^{-2} \sum_{i,j} \langle b_{i\uparrow}^\dagger b_{j\downarrow} \rangle e^{i\vec{k}\cdot(\vec{R}_i - \vec{R}_j)}, \tag{7}$$

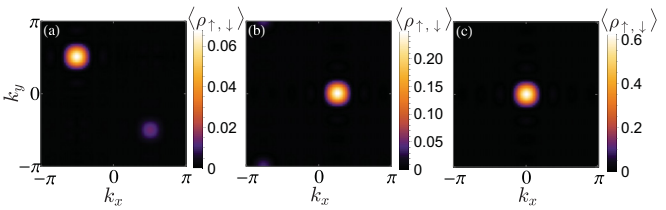

FIG. 5. Spin-dependent momentum distribution, Eq. (7), for different superfluids at $U_{\uparrow\downarrow} = 0.5U$, $\lambda = 0.04U$, $\mu = 1.33U$, (a) $t = 0.005U$, and (b) $t = 0.05U$.

where the lattice spacing is chosen as the unit of distance and $\vec{R}_j$ is the location of the lattice site j.

We take random initial guess states and minimize the total energy to compute the ground state $|G\rangle$, with which the spin-dependent momentum distribution is computed as $\langle G|\rho_{\uparrow,\downarrow}(\vec{k})|G\rangle/\langle G|G\rangle$. We get four degenerate ground states with different momentum distributions, where the D_4 symmetry of the lattice system is spontaneously broken. Similar results have been discovered in the continuum model of a spin-1/2 Bose-Einstein condensate with Rashaba SOC [56–58], where the ground state is a single plane-wave state with finite momentum, and the direction of plane wave is spontaneously determined when the interspin interaction is smaller than the intraspin interaction.

The two different states in Fig. 5 have qualitatively distinct momentum distributions. We have also verified that in these two phases, the magnitude of the order parameter is uniform over the whole lattice, indicating that only the phase pattern changes during the transition. Note that the peak in the momentum distribution for the first two phases depends strongly on the ratio between λ and t. In the noninteracting limit, the ground -state energy of the system with SOC is $E = -2t(\cos k_x + \cos k_y) - 2\lambda\sqrt{\sin^2 k_x + \sin^2 k_y}$. The energy minima are located at $\mathbf{k} = [\pm\arctan(\lambda/\sqrt{2}t), \pm\arctan(\lambda/\sqrt{2}t)]$. On a finite 8×8 lattice, $\mathbf{k}$ can only take discrete values. In particular, for $\lambda/t = 0.8$, the energy minima are located at $(0,\pi/4)$, $(0, -\pi/4)$, $(\pi/4,0)$, and $(-\pi/4,0)$. In the presence of interactions, D_4 symmetry is spontaneously broken and the system chooses one of the minima in Fig. 5(b). Similarly, for $\lambda/t = 8$, the energy minima are $\mathbf{k} = (\pm\pi/2, \pm\pi/2)$, which is consistent with Fig. 5(a). It is therefore possible to directly infer their ratio from the position of the peaks. We also note that the results presented in Fig. 5 relate directly to the time-of-flight imaging that can measure momentum distribution of distinct hyperfine states.

IV. QUANTUM PHASES IN A TRAPPING POTENTIAL

We now consider the effects of realistic confinement on the superfluid transitions. The finite momentum superfluids considered here are akin to the FFLO phase discussed in the context of trapped atomic Fermi gases. The FFLO state depends strongly on lattice geometry. Finite-size effects are normally not considered to be relevant in solids because system sizes are typically much larger than correlation lengths. But cold atomic gases can be put into regimes where the system size is on the order of superfluid correlation lengths.

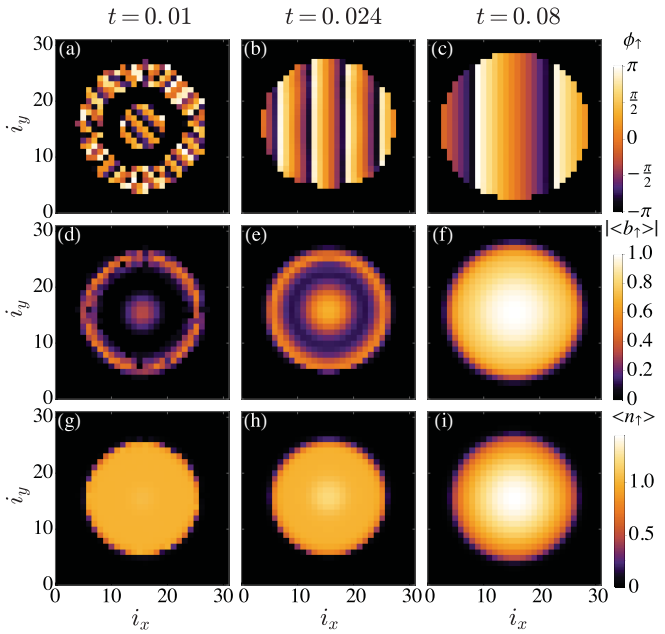

FIG. 6. Correlation functions of finite momentum superfluids on a 32×32 lattice with a confining potential [Eq. (8)] for $\mu = 0.8U$, $U_{\uparrow\downarrow} = 0$, and $\lambda = 0.04U$. The left column shows results for $t = 0.01U$, the middle column for $t = 0.024U$, and the right column for $t = 0.08U$. The top three panels plot the phase $\phi_\uparrow$ of the spin-up superfluid order parameter. The middle three panels plot the magnitude and the bottom three panels plot the density. The phase patterns in the top two panels reveal a sudden change in superfluid order.

Small magneto-optical trapping potentials can be created in cold-atom systems. We add a spatially varying chemical potential term to Eq. (2) to model confinement: $\sum_i V(\vec{R}_i)(n_{i,\uparrow} + n_{i,\downarrow})$. The trapping potentials are well approximated by a parabolic potential. We consider

$$V(\vec{R}_i) = 0.008U\left[\left(R_i^x - \frac{L_x - 1}{2}\right)^2 + \left(R_i^y - \frac{L_y - 1}{2}\right)^2\right], \tag{8}$$

where R_i^x (R_i^y) is the x (y) coordinate of site i and L_x (L_y) is the lattice size along the x (y) direction. The trap coefficient is chosen to ensure that the trapped atom density vanishes before the edge of the lattice is reached. Within the mean-field theory, we can compute the local superfluid order parameter in the trap $\langle b_{i,\sigma}\rangle = \sum_n \sqrt{n} f_{n-1}^{(i,\sigma)*} f_n^{(i,\sigma)}$. The local density is obtained as $\langle n_{i,\sigma}\rangle = \sum_n n|f_n^{(i,\sigma)}|^2$.

We now show that the phase change, discussed in the periodic systems above, also manifests in trapped systems. Figure 6 shows a typical example obtained from solving Eq. (2) in the presence of parabolic trapping using the Gutzwiller ansatz with 10^4 random initial guess states. Since a Mott insulator is an incoherent state with random phases, phases of up-arrow superfluid order parameter with $|\langle b_\uparrow\rangle| \leqslant 0.05$ are plotted with dark gray color in the top panel of Fig. 6. As the hopping parameter increases, the phase reorients in the trap from a nonuniform pattern to a uniform pattern due to the SOC effect. The effects predicted here are observable in measurements sensitive to the phase of the superfluid order parameter (e.g., the momentum distribution function). This calculation shows that realistic trapping potentials lead to finite-sized systems that harbor the transitions found in periodic systems discussed above.

V. QUANTUM PHASES IN INFINITE LATTICES

So far our study has been limited to finite-sized lattices. Here boundary effects put a strong constraint on the superfluid phase patterns that can be realized. But we can use Eq. (4) to study infinite lattices. We find a general solution for the lowest-energy state, $\theta_{i\uparrow} = \alpha(R_i^y - R_i^x)$ and $\theta_{i\downarrow} = \frac{\pi}{4} + \alpha(R_i^y - R_i^x)$, where $\alpha = \arctan(\lambda\sqrt{2}/2t)$. The corresponding energy for just the kinetic terms is

$$E_k = -(tA + \lambda B)\psi^2. \tag{9}$$

The competing superfluids arise from the competition between A and B coefficients.

Before studying the infinite system case, we first test that Eq. (9) gives the same results as the Gutzwiller mean-field theory. We find that this is the case by comparing results obtained from maximizing $tA + \lambda B$ in Eq. (9) on a finite lattice with the Gutzwiller mean-field theory. We find precisely the same phase patterns given in Fig. 5. This confirms that the Gutzwiller mean-field theory is equivalent to Eq. (9) on finite lattices.

We now study infinite lattice sizes. In the infinite system size limit we find $E_k \to -4\sqrt{2}\lambda \sin(\alpha) - 8t\cos(\alpha)$. This implies that the energy will change smoothly as the period of the finite momentum superfluids changes dramatically. Figure 7 shows that the energy computed on the infinite system size is in fact smooth. We therefore conclude that infinite lattice sizes will eliminate transitions observed in finite-sized systems. A similar result was found in studies of FFLO superfluids where periodic boundaries also constrain the FFLO momentum to select certain values [59,60]. But we note that realistic experiments are actually trapped finite-sized systems with $N \sim 10^2$–10^5. We therefore conclude that transitions between distinct superfluids found here should be observable in the small system limit defined by the trap center.

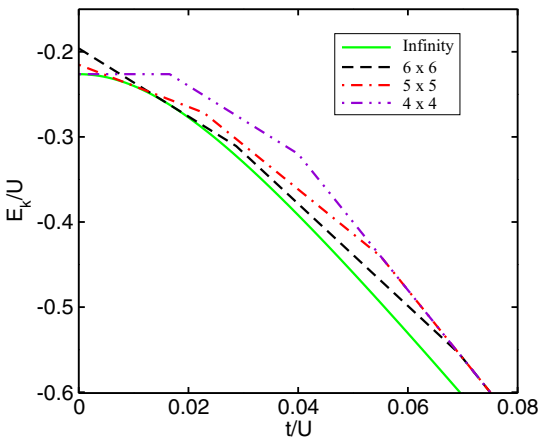

FIG. 7. Plot of the kinetic-energy terms, Eq. (9), as a function of the spin-independent tunneling at $\lambda = 0.04U$, for a 4×4, 5×5, 6×6 lattice and an infinite-size lattice.

VI. SUMMARY

We have studied the interplay of strong interaction and Rashba SOC in a model motivated by optical lattice experiments: a 2D Hubbard model of two-component bosons. We used mean-field theory to map out the phase diagram and study transitions. We find that strong Rashba SOC can completely destroy the Mott insulator state, even in the absence of spin-independent tunneling in the lattice. The Rashba SOC leads to superfluids with complex phase patterns and finite momentum. We identified transitions between superfluids with two different staggered phase patterns, that can be identified in the spin-dependent momentum distribution. The spin-dependent momentum could be accessed in time-of-flight measurements on optical lattices. We expect these transitions to occur in finite-sized systems but the phase patterns and precise momenta depend strongly on the boundaries. We checked that these transitions in phase patterns become smooth in infinite system sizes.

Our work relates to the nature of Mott insulator states in solids. Our study of a 2D lattice finds that it is in principle possible for strong Rashba SOC to convert a Mott insulator into a conducting state even in the limit of vanishing kinetics ($t \to 0$ with $\lambda \sim 1$ in the lattice model or $\langle p \rangle \to 0$ with $\langle \vec{\nabla} V \times \vec{p} \rangle \sim E_F$ in the continuum). This limit could have bearing on the nature of 3D Mott insulator surface states that experience very weak kinetics but strong electric fields.

ACKNOWLEDGMENTS

Y.Q., V.S., and C.Z. are supported by ARO (W911NF-12-1-0335, W911NF-16-1-0182, W911NF-17-1-0128), AFOSR (FA9550-11-1-0313, FA9550-15-1-0445, FA9550-16-1-0387), NSF-PHY (1505496), and DARPA-YFA. M.G. is supported in part by Hong Kong RGC/GRF Project 401512, the Hong Kong Scholars Program (Grant No. XJ2011027), and the Hong Kong GRF Project 2130352.

[1] E. I. Rashba, Sov. Phys. Solid State **2**, 1109 (1960).
[2] G. Nicolay, F. Reinert, S. Hufner, and P. Blaha, Phys. Rev. B **65**, 033407 (2001).
[3] G. Bihlmayer, S. Blugel, and E. V. Chulkov, Phys. Rev. B **75**, 195414 (2007).
[4] R. Winkler, *Spin-Orbit Coupling Effects in Two-Dimensional Electron and Hole Systems*, Springer Tracts in Modern Physics (Springer, Berlin, 2003).
[5] M. Z. Hasan and C. L. Kane, Rev. Mod. Phys. **82**, 3045 (2010).
[6] X. Qi and S. C. Zhang, Rev. Mod. Phys. **83**, 1057 (2011).
[7] Y.-J. Lin, K. Jimenez-Garcia, and I. B. Spielman, Nature (London) **471**, 83 (2011).
[8] P. Wang, Z. Q. Yu, Z. Fu, J. Miao, L. Huang, S. Chai, H. Zhai, and J. Zhang, Phys. Rev. Lett. **109**, 095301 (2012).
[9] L. W. Cheuk, A. T. Sommer, Z. Hadzibabic, T. Yefsah, W. S. Bakr, and M. W. Zwierlein, Phys. Rev. Lett. **109**, 095302 (2012).
[10] J. Y. Zhang, S. C. Ji, Z. Chen, L. Zhang, Z. D. Du, B. Yan, G. S. Pan, B. Zhao, Y. J. Deng, H. Zhai, S. Chen, and J. W. Pan, Phys. Rev. Lett. **109**, 115301 (2012).
[11] Z. Fu, L. Huang, Z. Meng, P. Wang, X. J. Liu, H. Pu, H. Hu, and J. Zhang, Phys. Rev. A **87**, 053619 (2013).
[12] C. Qu, C. Hamner, M. Gong, C. Zhang, and P. Engels, Phys. Rev. A **88**, 021604(R) (2013).
[13] R. A. Williams, M. C. Beeler, L. J. LeBlanc, K. Jimenez-Garcia, and I. B. Spielman, Phys. Rev. Lett. **111**, 095301 (2013).
[14] I. Bloch, J. Dalibard, and W. Zwerger, Rev. Mod. Phys. **80**, 885 (2008).
[15] V. Galitski and I. B. Spielman, Nature (London) **494**, 49 (2013).
[16] J. D. Sau, R. Sensarma, S. Powell, I. B. Spielman, and S. Das Sarma, Phys. Rev. B **83**, 140510(R) (2011).
[17] Y. Zhang and C. Zhang, Phys. Rev. A **87**, 023611 (2013).
[18] F. Lin, C. Zhang, and V. W. Scarola, Phys. Rev. Lett. **112**, 110404 (2014).
[19] H.-Y. Hui, Y. Zhang, C. Zhang, and V. W. Scarola, Phys. Rev. A **95**, 033603 (2017).
[20] M. Chen and V. W. Scarola, Phys. Rev. A **94**, 043601 (2016).
[21] H. Hu, B. Ramachandhran, H. Pu, and X. J. Liu, Phys. Rev. Lett. **108**, 010402 (2012); B. Ramachandhran, H. Hu, and H. Pu, Phys. Rev. A **87**, 033627 (2013).
[22] C. Wu, I. Mondragon-Shem, and X. Zhou, Chin. Phys. Lett. **28**, 097102 (2011); X. Zhou, Y. Li, Z. Cai, and C. Wu, J. Phys. B **46**, 134001 (2013).
[23] B. Ramachandhran, B. Opanchuk, X.-J. Liu, H. Pu, P. D. Drummond, and H. Hu, Phys. Rev. A **85**, 023606 (2012).
[24] J. Radic, A. Di Ciolo, K. Sun, and V. Galitski, Phys. Rev. Lett. **109**, 085303 (2012).
[25] W. S. Cole, S. Z. Zhang, A. Paramekanti, and N. Trivedi, Phys. Rev. Lett. **109**, 085302 (2012).
[26] Z. Cai, X. Zhou, and C. Wu, Phys. Rev. A **85**, 061605(R) (2012).
[27] S. Mandal, Kush Saha, K. Sengupta, Phys. Rev. B **86**, 155101 (2012).
[28] M. Gong, Y. Qian, M. Yan, V. W. Scarola, and C. Zhang, Sci. Rep. **5**, 10050 (2015).
[29] I. Vurgaftman, J. R. Meyer, and L. R. Ram-Mohan, J. Appl. Phys. **89**, 5815 (2001).
[30] J. B. Miller, D. M. Zumbuhl, C. M. Marcus, Y. B. Lyanda-Geller, D. Goldhaber-Gordon, K. Campman, and A. C. Gossard, Phys. Rev. Lett. **90**, 076807 (2003).
[31] M. Oestreich and W. W. Ruhle, Phys. Rev. Lett. **74**, 2315 (1995).
[32] G. L. Chen, J. Han, T. T. Huang, S. Datta, and D. B. Janes, Phys. Rev. B **47**, 4084 (1993).
[33] H. Kosaka, A. A. Kiselev, F. A. Baron, K. W. Kim, and E. Yablonovitch, Electron. Lett. **37**, 464 (2001).
[34] S. K. Greene, J. Singleton, P. Sobkowicz, T. D. Golding, M. Pepper, J. Perenboom, and J. Dinan, Semicond. Sci. Technol. **7**, 1377 (1992).
[35] K. Michaeli, A. C. Potter, and P. A. Lee, Phys. Rev. Lett. **108**, 117003 (2012).
[36] P. Fulde and R. A. Ferrell, Phys. Rev. **135**, A550 (1964).
[37] A. I. Larkin, and Yu. N. Ovchinnikov, Zh. Eksp. Teor. Fiz. **47**, 1136 (1964) [Sov. Phys. JETP **20**, 762 (1965)].
[38] Z. Cai, Y. Wang, and C. Wu, Phys. Rev. A **83**, 063621 (2011).

[39] R. Casalbuoni and G. Nardulli, Rev. Mod. Phys. **76**, 263 (2004).
[40] T. Mizushima, M. Ichioka, and K. Machida, J. Phys. Chem. Solids **66**, 1359 (2005).
[41] H. Hu, X. J. Liu, and P. D. Drummond, Phys. Rev. Lett. **98**, 070403 (2007).
[42] T. K. Koponen, T. Paananen, J.-P. Martikainen, M. R. Bakhtiari, and P. Törmä, New J. Phys. **10**, 045014 (2008).
[43] A. E. Feiguin and F. Heidrich-Meisner, Phys. Rev. B **76**, 220508(R) (2007).
[44] T. Paananen, J. Phys. B **42**, 165304 (2009).
[45] M. M. Parish, S. K. Baur, E. J. Mueller, and D. A. Huse, Phys. Rev. Lett. **99**, 250403 (2007).
[46] J. Tempere, M. Wouters, and J. T. Devreese, Phys. Rev. B **75**, 184526 (2007).
[47] Y. L. Loh and N. Trivedi, Phys. Rev. Lett. **104**, 165302 (2010).
[48] D. Jaksch, C. Bruder, J. I. Cirac, C. W. Gardiner, and P. Zoller, Phys. Rev. Lett. **81**, 3108 (1998).
[49] D. S. Rokhsar and B. G. Kotliar, Phys. Rev. B **44**, 10328 (1991).
[50] V. W. Scarola and S. Das Sarma, Phys. Rev. Lett. **98**, 210403 (2007).
[51] J. Zakrzewski, Phys. Rev. A **71**, 043601 (2005).
[52] A. E. Niederle and H. Rieger, New J. Phys. **15**, 075029 (2013).
[53] P. Debye, Math. Ann. **67**, 535 (1909).
[54] P. Deift and X. Zhou, Ann. Math. **137**, 295 (1993).
[55] M. P. A. Fisher, P. B. Weichman, G. Grinstein, and D. S. Fisher, Phys. Rev. B **40**, 546 (1989).
[56] C. J. Wang, C. Gao, C. M. Jian, and H. Zhai, Phys. Rev. Lett. **105**, 160403 (2010).
[57] T.-L. Ho and S. Zhang, Phys. Rev. Lett. **107**, 150403 (2011).
[58] Y. Li, L. P. Pitaevskii, and S. Stringari, Phys. Rev. Lett. **108**, 225301 (2012).
[59] A. V. Samokhvalov, A. S. Melnikov, and A. I. Buzdin, Phys. Rev. B **82**, 174514 (2010).
[60] J. P. A. Devreese, M. Wouters, and J. Tempere, Phys. Rev. A **84**, 043623 (2011).